

Near-field acoustic imaging with a caged bubble

Dorian Bouchet,¹ Olivier Stephan,¹ Benjamin Dollet,¹ Philippe Marmottant,¹ and Emmanuel Bossy¹

¹*Université Grenoble Alpes, CNRS, LIPhy, 38000 Grenoble, France*

Bubbles are ubiquitous in many research applications ranging from ultrasound imaging and drug delivery to the understanding of volcanic eruptions and water circulation in vascular plants. From an acoustic perspective, bubbles are resonant scatterers with remarkable properties, including a large scattering cross-section and strongly sub-wavelength dimensions. While it is known that the resonance properties of bubbles depend on their local environment, it remains challenging to probe this interaction at the single-bubble level due to the difficulty of manipulating a single resonating bubble in a liquid. Here, we confine a cubic bubble inside a cage using 3D printing technology, and we use this bubble as a local probe to perform scanning near-field acoustic microscopy—an acoustic analogue of scanning near-field optical microscopy. By probing the acoustic interaction between a single resonating bubble and its local environment, we demonstrate near-field imaging of complex structures with a resolution that is two orders of magnitudes smaller than the wavelength of the acoustic field. As a potential application, our approach paves the way for the development of low-cost acoustic microscopes based on caged bubbles.

INTRODUCTION

Scanning near-field optical microscopy (SNOM) is an invaluable tool for the study of light-matter interaction in the optical regime [1]. Following the original proposition of Synge in 1928 [2] and the development of aperture-type microscopes [3], SNOM has been demonstrated with a variety of sub-wavelength probes such as metallic tips [4], gold particles [5] and fluorescent molecules [6]. This allows not only to reconstruct images of samples with a sub-wavelength resolution [7], but also to investigate electromagnetic interactions at the nanoscale, for instance to study single-molecule fluorescence in the vicinity of photonic antennas [8, 9] and to map the local density of optical states close to nanostructured materials [10–12].

For many applications in nondestructive testing and biological imaging [13, 14], it is necessary to be specifically sensitive to the elastic properties of materials. In this context, it is thus relevant to use acoustic waves instead of light as a sensing mechanism. In the acoustic regime, probing near-field interactions entails using acoustic resonators instead of optical emitters. Acoustic interactions can be probed using different types of resonators such as a tuning fork [15], a cantilever [16], a Chinese gong [17], or a nanoparticle [18]. However, further advances in scanning near-field acoustic microscopy (SNAM) are hindered by the difficulty of finding local probes that can be easily manipulated, that strongly interact with the acoustic field, and that are sub-wavelength along all dimensions. Gas bubbles are excellent candidates for this application, thanks to their large scattering cross-section and their strongly sub-wavelength dimensions [19, 20]. As such, ensembles of bubbles freely flowing inside blood vessels have been used to reconstruct super-resolved images by ultrasound localization microscopy [21]—an acoustic analogue of photo-activated localization microscopy [22, 23]. However, in order to use a single resonating bubble as a local probe for SNAM, one needs to scan the position of the bubble in three dimensions. First steps in this direction have been achieved by attaching an oil droplet to the can-

tilever of an atomic force microscope [24, 25], an idea that has then be applied to the characterization of interaction forces between an air bubble and its surrounding environment [26–29]. Another manipulation strategy consists in using optical tweezers to trap single bubbles, a technique that has been used to experimentally observe changes in microbubble dynamics close to interfaces [30, 31].

Here, we harness the possibility to manipulate a resonating acoustic bubble inside a cage using 3D printing technology [32, 33] and experimentally demonstrate that this bubble can be used as a local probe for SNAM (Fig. 1). By measuring variations in the resonance properties of the bubble induced by near-field acoustic interactions, we reconstruct images of structured samples with a resolution that is not limited by diffraction but by the size of the bubble, which is two order of magnitudes smaller than the wavelength of the acoustic field. The method offers different contrast mechanisms, as the various resonance parameters of the bubble (such as its resonance amplitude or its resonance frequency) are influenced by the acoustic impedance of the surrounding environment in a specific way. By demonstrating a SNAM approach based on a single resonating bubble, we thus introduce a tool to determine acoustic properties of structured materials at the sub-wavelength scale.

RESULTS

Principle of the experiment

Following a mechanical excitation by an acoustic wave, a gas bubble in a liquid behaves as a resonant scatterer, as its volume oscillates about an equilibrium value. For a spherical bubble, the resonance frequency is given by the Minnaert formula $f_0 = c_g \sqrt{3\rho_g/\rho_l}/(\pi d_0)$ where c_g is the speed of sound in the gas, ρ_g and ρ_l are the densities of the gas and the liquid, and d_0 is the diameter of the bubble at equilibrium [19]. At resonance, the ratio between the wavelength λ of acoustic waves in the liquid

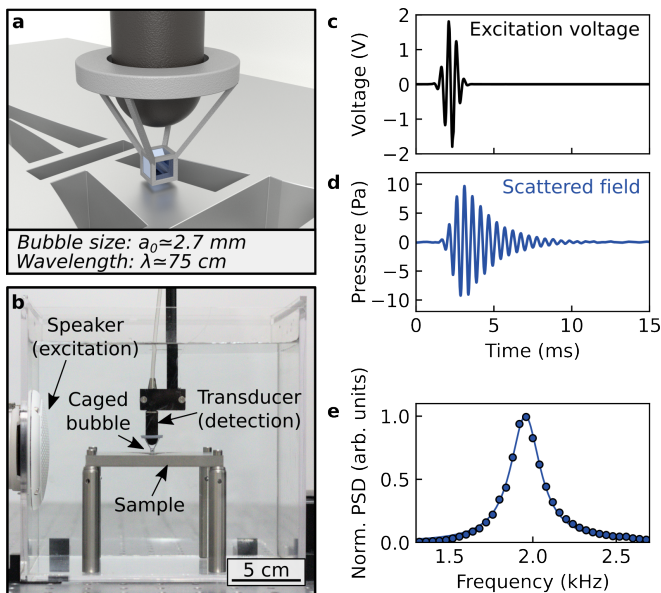


FIG. 1. Principle of a scanning near-field acoustic microscope based on a caged bubble. **a**, Artistic representation of a cubic bubble confined inside a 3D-printed cage placed at the tip of a hydrophone. **b**, Photograph of the experiment. A caged bubble, whose position is controlled with a 3D motorized stage, is scanned in the near field of a structured sample. The resonance of the bubble is excited by an acoustic pulse generated using a speaker, and the scattered field is recorded by a transducer connected to the 3D-printed cage. **c**, Excitation voltage supplied to the speaker. **d**, Field scattered by the bubble in the absence of sample. **e**, Normalized power spectral density (PSD) of the field measured in the absence of sample (blue dots), along with a Lorentzian fit to the data (blue line).

and the diameter of the bubble is thus

$$\frac{\lambda}{d_0} = \frac{\pi c_l}{c_g} \sqrt{\frac{\rho_l}{3\rho_g}}, \quad (1)$$

where c_l is the speed of sound in the liquid. For an air bubble in water at 20°C, Eq. (1) yields $\lambda/d_0 = 226$. As such, an air bubble in water is inherently a strongly sub-wavelength resonant scatterer, and thus constitutes an ideal local probe for the acoustic field.

To experimentally demonstrate how a single bubble can be used for SNAM, we built a millimetric cubic cage using a 3D printing technique based on digital light processing. A commercial resin is polymerized using a 3D printer, and a water-repellent treatment is applied to ensure an efficient hydrophobicity of the cage (see Methods for a detailed description of the fabrication of the cages). When immersed into a water tank, this cage confines and stabilizes an air bubble, as illustrated in Fig. 1a. Indeed, for cage lengths up to a few millimeters, the surface tension induced by the hydrophobicity of the cage overcomes the hydrostatic pressure induced by gravity, thereby preventing water from entering inside the cage. The position of such a bubble is then easily controlled in three dimen-

sions by moving the cage using a motorized stage. The cubic geometry of the bubbles has been chosen for its simplicity of fabrication, but other bubble shapes could also be considered [34, 35]. The resonance frequency of a cubic bubble of side length a_0 is essentially driven by the volume V of the gas in the bubble, as previously investigated using bubbles of polyhedral shapes [34]. Using a diameter $d_0 = 2a_0[3/(4\pi)]^{1/3}$ in Eq. (1), we obtain $\lambda/a_0 = 280$, evidencing that cubic bubbles in water are also strongly sub-wavelength resonators, in the same way as spherical ones.

To probe this resonance experimentally, we excite the bubble externally with a broadband pulse generated by an underwater loudspeaker, and we measure the acoustic signal using a transducer located in the vicinity of the bubble (Fig. 1b,c, see also Methods). In all experiments, we first measure the pressure field in the presence of the bubble $\phi_w(\mathbf{r}, t)$ (i.e., with air inside the cage), and we then measure the field in the absence of the bubble $\phi_{w/o}(\mathbf{r}, t)$ (i.e., with water inside the cage, which is achieved by replacing air by water by use of a pipette). The field scattered by the bubble is then defined as $\phi_s(\mathbf{r}, t) = \phi_w(\mathbf{r}, t) - \phi_{w/o}(\mathbf{r}, t)$. From these time-resolved measurements (Fig. 1d), we then calculate the normalized power spectral density $|A_s(\mathbf{r}, \omega)|^2 = |\hat{\phi}_s(\mathbf{r}, \omega)/\hat{\phi}_{w/o}(\mathbf{r}, \omega)|^2$, which is the frequency spectrum of the scattered field deconvolved by the excitation signal. Such a spectrum is well described by a Lorentzian function (Fig. 1e), with a quality factor around 10. All experiments are performed with an external cage size of 3 mm ($V \simeq 20$ mm³, $a_0 \simeq 2.7$ mm), for which a resonance frequency of 1.9 kHz is predicted by the Minnaert formula. In practice, the observed resonance frequency typically lies between 1.9 kHz and 2.0 kHz, indicating that small deviations can occur in the volume of air trapped within the cage. Once a bubble is confined inside a cage, it remains stable for several hours, and the small decrease of air volume that occurs over long measurement times can be easily corrected for using a linear correction (see Supplementary Materials, Section S1).

Bubble dynamics close to an interface

The resonance of a bubble is known to convey information about the acoustic impedance of its surrounding environment [20]. To demonstrate the possibility of measuring these acoustic interactions with a caged bubble in water, we study the canonical situation of a single resonating bubble whose center is located at a controlled distance z from an interface. We first experimentally investigate the case of a bubble close to a water-steel interface (Fig. 2a), which approximates a Neumann boundary condition (BC) for the pressure (zero normal velocity). In this case, a negative frequency shift is observed close to the interface (Fig. 2b,c). For comparison purposes, we then investigate the case of a water-air interface (Fig. 2e), which approximates a Dirichlet BC (pressure-free inter-

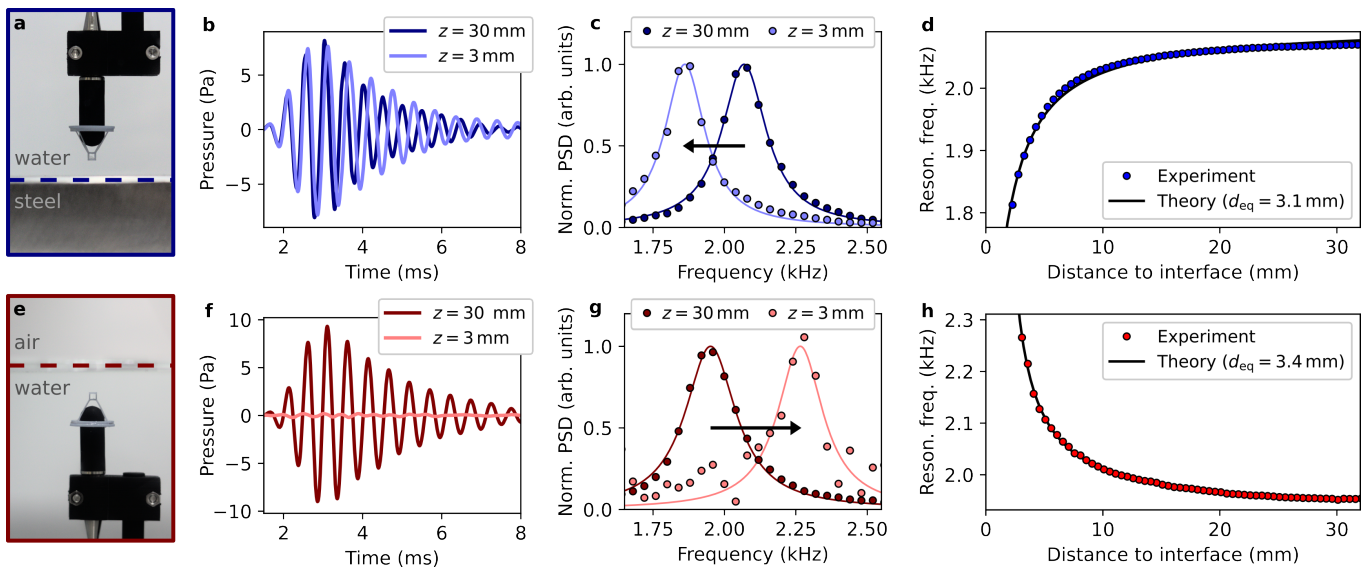


FIG. 2. Measurements of the bubble dynamics close to interfaces. **a**, Photograph of the experiment, in which a caged bubble is scanned in the vertical direction above a water-steel interface (blue dashed line). **b**, Field scattered by the bubble in the vicinity of the interface ($z = 3$ mm, light blue) and far from the interface ($z = 30$ mm, dark blue). The resonance frequency is visibly reduced close to the interface. **c**, Normalized power spectral density of the scattered field when the bubble is in the vicinity of the interface ($z = 3$ mm, light blue) and far from the interface ($z = 30$ mm, dark blue). **d**, Experimental measurements of the resonance frequency of the bubble as a function of the distance to the interface (blue points), along with theoretical predictions given by Eq. (2). **e-h**, Analogous to **a-d** for a caged bubble scanned below a water-air interface. In the vicinity of the interface, the measured field is very weak (**f**), but the frequency shift experienced by the bubble can still be observed (**g**). As theoretically predicted by Eq. (2), the behavior of the resonance frequency is different in the case of a water-air interface (the resonance frequency increases) and in the case of a water-steel interface (the resonance frequency decreases).

face). The amplitude of the measured field close to the interface is strongly reduced (Fig. 2f), but the spectral analysis does reveal a positive frequency shift close to the interface (Fig. 2g).

Different approaches can be considered to theoretically determine variations in the resonance properties of the bubble due to the presence of the interface. One such approach is to solve a modified Rayleigh-Plesset equation describing the oscillation of a bubble near an elastic wall [36]. To model our experiments, in which bubbles are placed in the near field of rigid and free interfaces, we will rather use the exact expression derived by Morioka based on the potential flow of an incompressible liquid around two spherical bubbles [37]:

$$f_{\pm}/f_0 = \sqrt{\sum_{n=0}^{+\infty} \frac{(\mp 1)^n \sinh(\beta)}{\sinh[(n+1)\beta]}}, \quad (2)$$

where $\cosh(\beta) = 2z/d_0$, and where f_+ and f_- denote the resonance frequency of two in-phase and out-of-phase bubbles, respectively. Using the method of images, f_+ and f_- are found to be also the resonance frequency of a single bubble close to rigid (Neuman BC) and free (Dirichlet BC) interfaces, respectively [19]. Note that, for $z \gg d_0/2$, this expression matches the approximate solution obtained by Strasberg [38], which is $f_{\pm}/f_0 =$

$$1/\sqrt{1 \pm d_0/(4z)}.$$

While Eq. (2) describes the case of a spherical bubble close to an interface separating two semi-infinite media, our experiments involve a cubic bubble inside a tank of finite dimensions. Therefore, in order to compare our experimental results to those predicted by the theory, we need to study how the resonance frequency of the bubble is influenced by the cubic geometry of the bubble and by the presence of the tank. For this purpose, we conducted 3D numerical simulations based on a finite-difference time-domain (FDTD) solver of the elastodynamic equations [39] (see Methods). We considered the case of a tank filled with water (same dimensions as in the experiments) containing a cubic air bubble close to rigid and free interfaces. As expected, we observed that the bubble radiates much more in the vicinity of a rigid interface (Fig. 3a) as compared to a free interface (Fig. 3b). We then calculated the evolution of its resonance frequency as a function of the bubble-interface distance. However, in order to compare these results to the theory expressed by Eq. (2), we needed to determine an effective diameter for a cubic bubble of edge size a_0 . While taking $d_{\text{eq}} = 2a_0[3/(4\pi)]^{1/3}$ based on the volume of air enclosed in the bubble would be a good approximation (see Supplementary Materials, Section S2.1), a better agreement was obtained by considering the effective diameter as a free parameter. Using this procedure, FDTD results are

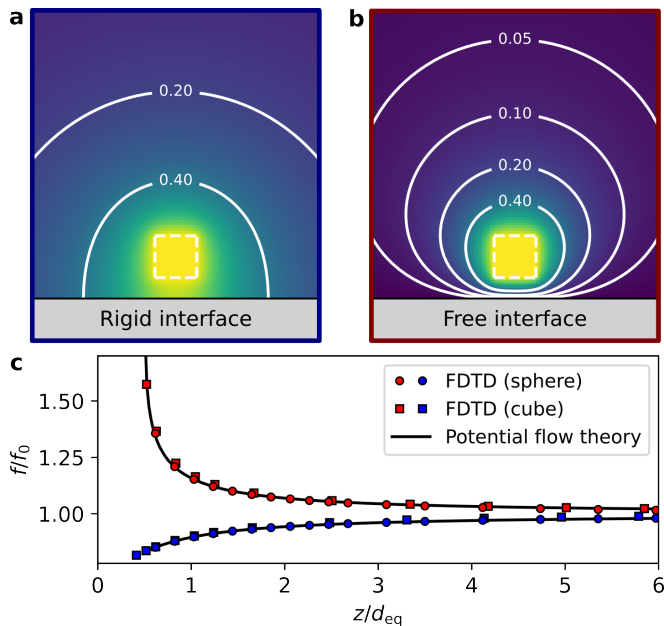


FIG. 3. Modeling of the bubble dynamics close to interfaces. **a,b**, Normalized instantaneous pressure fields calculated by FDTD around a cubic bubble close to a rigid interface (**a**) and a free interface (**b**). On these figures, the edges of the bubble are represented by dotted white lines (edge size of 2.5 mm). **c**, Relation between the normalized resonance frequency f/f_0 and the normalized bubble-interface distance z/d_{eq} for rigid (in blue) and free (in red) interfaces. Theoretical predictions obtained using Eq. (2) are represented by black lines. Results of FDTD simulations performed with a spherical bubble in water surrounding by perfectly-matched layers are represented by blue and red circles (with d_{eq} being taken as the true diameter of the bubble). Results of FDTD simulations performed with a cubic bubble in water enclosed in a finite tank are represented by blue and red squares (with d_{eq} obtained by fitting FDTD results to the predictions of Eq. (2)).

accurately described by theoretical predictions obtained with Eq. (2) (Fig. 3c). In the experiments, both the effective bubble diameter and the minimal bubble-interface distance need to be treated as free parameters (see Supplementary Materials, Section 6). Using this procedure, we observed again an excellent agreement between theoretical predictions and experimental results (Fig. 2d,h). This shows that we can neglect the influence of the (non-resonant) tank, evidencing that the bubble resonance frequency is mostly sensitive to the extreme near-field of the bubble ($z \ll \lambda$). Furthermore, this also demonstrates that the resonance frequency of a cubic bubble close to an interface behaves very similarly to that of a spherical one. This can be understood from the similar pressure fields emitted by spherical and cubic bubbles (see Supplementary Materials, Section S2.2), which are essentially those that would be generated by two in-phase monopoles (rigid interface) or two out-of-phase monopoles (free interface).

Super-resolved near-field images

Beyond 1D line scans in the z -direction, we also demonstrate the possibility to reconstruct super-resolved 2D images by scanning the bubble in the xy -plane above structured samples. This procedure is illustrated in the supplementary movies (Movie M1 and Movie M2), in which one can hear the sound emitted by the bubble while watching images being built. The resonance of the bubble is characterized by several parameters, including the central frequency, the linewidth, the integrated signal energy, and the shape of the power spectrum. We can thus apply different imaging modalities, which yield different contrasts depending on the acoustic properties of the samples. Here, we perform intensity imaging, which consists in imaging the spatial dependence of the power spectral density at a given frequency (Fig. 4a). In addition, we also implement central frequency imaging, which consists in imaging the spatial dependence of the measured central frequency that is estimated from a Lorentzian fit to the power spectral density (Fig. 4b). We apply these approaches to a stainless-steel sample on which an artistic representation of the Eiffel tower is engraved (Fig. 4c). By scanning the bubble in the close vicinity of the sample (the distance between the center of the bubble and the surface of the sample is set to $z = 2.5$ mm) and by probing point-by-point the resonance of the bubble, we obtain super-resolved images of the sample (Fig. 4d,e), on which details as small as $\lambda/250$ (distance of 3 mm) can be distinguished. As expected, the measured resonance frequency decreases in the vicinity of stainless steel (Fig. 4e). Furthermore, the signal also decreases in the vicinity of stainless steel on the intensity image reconstructed at $f = 1.96$ kHz (Fig. 4d; intensity images for other frequencies are available in Supplementary Materials, Section S3.1). This is in fact a direct consequence of the frequency shift experienced by the bubble, as 1.96 kHz corresponds here to the resonance frequency of the bubble above the sample areas filled with water.

As evidenced in Fig. 2, the resonance of the bubble varies differently depending on the acoustic properties of the surrounding medium. Therefore, using a bubble as a local probe for SNAM enables one not only to recover spatial features of complex samples with a strongly sub-wavelength resolution, but also to access information about the acoustic properties of the samples. To illustrate this advantage, we study a sample with spatially heterogeneous properties (Fig. 4f): the SNAM acronym is engraved on a stainless-steel plate, with the letter “A” covered with adhesive tape before immersing the sample in water. In this way, this letter is filled with air, while other letters are filled with water. This difference of acoustic properties can clearly be observed on the reconstructed super-resolved images (Fig. 4g,h). As expected, the measured resonance frequency decreases in the vicinity of stainless steel and increases in the vicinity of air (Fig. 4h). In contrast, the signal decreases in the vicinity of air on the intensity image measured at $f = 1.96$ kHz

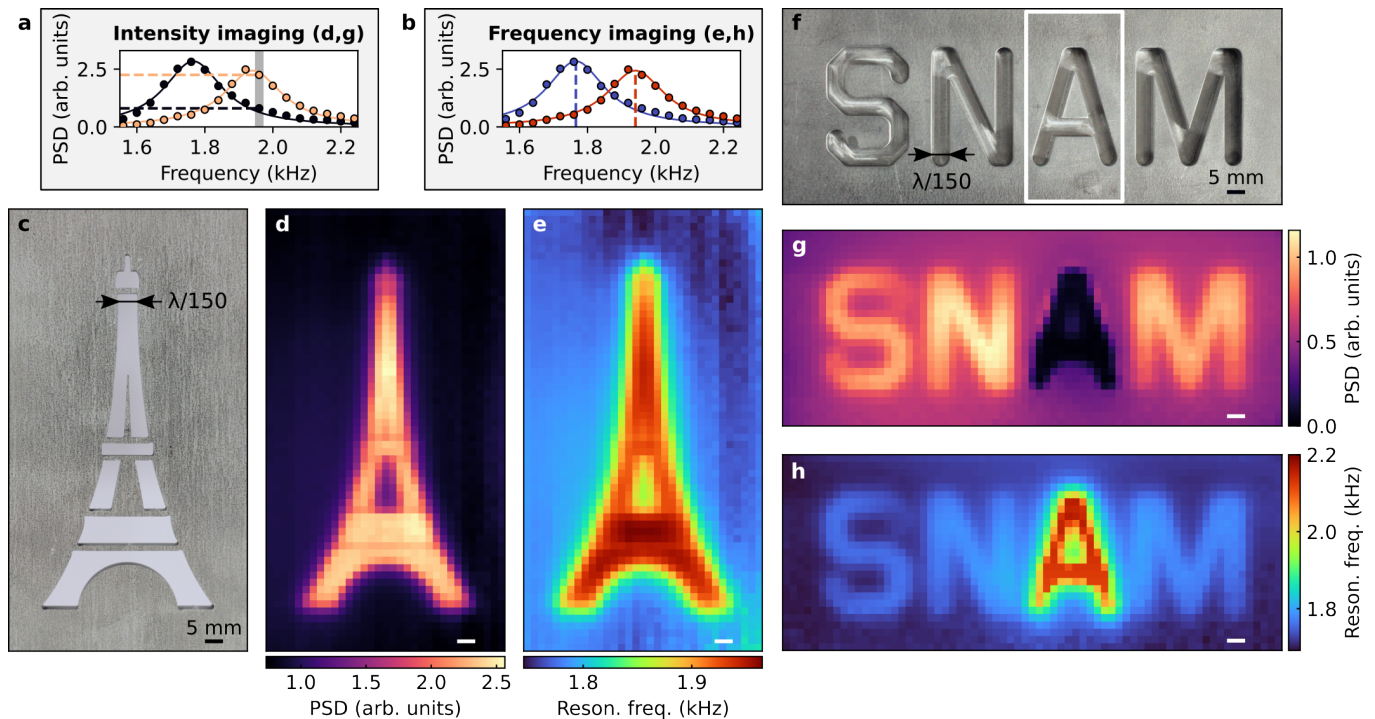


FIG. 4. Demonstration of super-resolution near-field imaging with a single resonating bubble. **a**, Illustration of the intensity imaging mode: a frequency is chosen (here $f = 1.96$ kHz) and an image is reconstructed based on the power spectral density measured at this frequency. **b**, Illustration of the central frequency imaging mode: an image is reconstructed based on measured central frequencies, that are estimated from a Lorentzian fit to the power spectral densities. **c**, Photograph of a stainless-steel sample on which an artistic representation of the Eiffel tower is engraved. The thickness of the plate is 8 mm, and engraved patterns go through the whole plate thickness. **d,e**, Super-resolved images obtained by scanning a caged bubble 2 mm above the sample shown in **c**, in the intensity imaging mode at $f = 1.96$ kHz (**d**) and in the central frequency mode (**e**). Instead of being limited by diffraction ($\lambda/2 \simeq 375$ mm), the resolution of the approach is given by the size of the bubble (3 mm), two orders of magnitude below the resolution limit. **f-h**, Analogous to **c-e** for a stainless-steel sample engraved with the SNAM (scanning near-field acoustic microscopy) acronym. The thickness of the plate is 8 mm, and patterns are engraved over a thickness of 7 mm. In the experiment, the letter “A” is covered with adhesive tape (white rectangle in **f**), in order to trap an air layer in the letter. The contrast of the resulting super-resolved images (**g,h**) varies depending on the acoustic properties of the sample (air for the letter “A”, water for other letters).

(Fig. 4g; intensity images for other frequencies are available in Supplementary Materials, Section S3.2). This is explained not only by the shift in the resonance frequency, but also by the decrease in the integrated signal energy measured from the bubble.

Transverse resolution

It is not straightforward to provide a quantitative measure of the resolution of the technique. The resolution of an image is often defined from the 2D point response function (PRF) of the system [40], but this function is not unique in our case as it depends on the third dimension of the system (the sample thickness) as well as on the imaging mode (intensity imaging or frequency imaging). For this reason, we adopt here an alternative approach inspired by Fourier ring correlation (FRC), a method which is commonly used in different research fields including

cryo-electron microscopy [41, 42] and single-molecule localization microscopy [43, 44]. This approach provides a systematic way to identify the maximal spatial frequency ξ for which the signal is significantly larger than the noise. The approach is implemented directly from raw experimental data, which are in our case the pressure fields measured in the presence of the bubble. Here, our resolution test sample is composed of three lines engraved in a stainless-steel plate, and we measure the resonance frequency of the bubble for different distances z (Fig. 5a). Spatial variations become less visible for larger values of z , which qualitatively evidences that the resolution rapidly degrades with the bubble-sample distance. This is confirmed quantitatively by our spectral analysis inspired by FRC (see Supplementary Materials, Section S4), which reveals a decrease of the maximal spatial frequency ξ with z (Fig. 5b) and therefore a degradation of the associated spatial resolution $\mathcal{R} = 1/\xi$ (Fig. 5c).

The relation between the distance z and the resolution

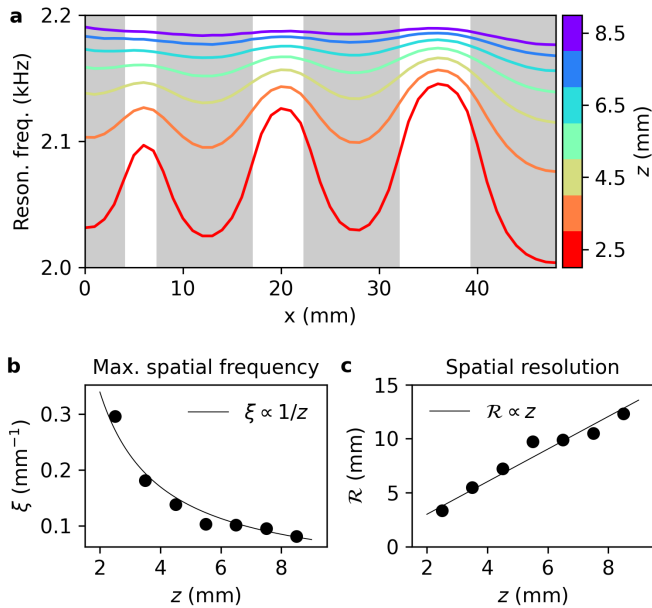


FIG. 5. Transverse resolution of the approach. **a**, Experimental measurements of the resonance frequency of the bubble for a 1D line scan above a resolution test sample composed of three lines (white bands in the figure) engraved in a stainless-steel plate (gray bands in the figure). The thickness of the plate is 8 mm, and engraved patterns go through the whole plate thickness. Performing these measurements for different distances z ranging from 2.5 mm (red curve) to 8.5 mm (purple curve) demonstrates that the resolution rapidly degrades with the bubble-sample distance. **b**, Maximum spatial frequency ξ measured in these 1D line scans as a function of the bubble-sample distance z (black points), along with a theoretical model predicting $\xi \propto 1/z$ (black curve). **c**, Spatial resolution $\mathcal{R} = 1/\xi$ measured in these 1D line scans as a function of the bubble-sample distance z (black points), along with the $\mathcal{R} \propto z$ prediction (black curve).

\mathcal{R} can be understood based on the angular spectrum representation of the pressure field [45]:

$$\phi_w(\mathbf{r}, t) = \frac{1}{4\pi^2} \iint \phi_w(k_x, k_y, z=0, t) \exp(i\mathbf{k} \cdot \mathbf{r}) dk_x dk_y, \quad (3)$$

where $\phi_w(k_x, k_y, z=0, t)$ is the spatial Fourier transform of $\phi_w(x, y, z=0, t)$ along the transverse dimensions (x and y), and where $\|\mathbf{k}\|^2 = k_x^2 + k_y^2 + k_z^2 = (2\pi/\lambda)^2$. Deeply sub-wavelength structured samples are described by transverse wavenumbers $k_{\parallel} = \sqrt{k_x^2 + k_y^2}$ that satisfy $k_{\parallel} \gg 2\pi/\lambda$, which results in $k_z \simeq ik_{\parallel}$ and therefore $\exp(ik_z z) \simeq \exp(-k_{\parallel} z)$. Consequently, in the deeply near-field regime, high transverse spatial frequencies are exponentially attenuated through propagation in the z direction, with an attenuation factor that scales with the transverse wavenumber. This is confirmed by our spectral analysis of experimental data, which shows that the maximal spatial frequency ξ scales with $1/z$ (Fig. 5b) and that the measured resolution \mathcal{R} scales with z (Fig. 5c).

In the close vicinity of the sample (for $z = 2.5$ mm), the measured resolution is approximately 3 mm, which is on the order of the bubble size.

DISCUSSION

While these experiments were performed here with millimetric bubbles for the sake of experimental simplicity, we emphasize that our proposed approach is inherently scalable: indeed, for a gas bubble in liquid, the size of the bubble is always much smaller than the wavelength of the scattered waves. This can be seen from Eq. (1), since typically $\rho_l \gg \rho_g$ and $c_l \gg c_g$. On the one hand, scaling up the size of the bubble cage in the centimeter range [34] would enable locally-resolved rheological measurements of interfaces in the few hundred Hz frequency range, otherwise impossible with diffraction-limited transducers which would be several meters in size. On the other hand, our approach could be implemented on the micrometer scale by engineering cages via 3D microfabrication [46], which would allow to reach a micrometer resolution using conventional MHz electronics and transducers. Current commercial acoustic microscopes, widely used for non-destructive testing in the industry and biomedical applications on the micrometer scale [14, 47], are based on expensive electronics and transducers working in the GHz range. Our approach would enable acoustic microscopy with micrometer resolution at the cost of a MHz ultrasound imaging system, that are typically one or two orders of magnitude cheaper than GHz systems. Towards this goal, a challenge will be to stabilize micrometer-scale bubble and counteract the loss of air dissolving into the water, which could be done either with a coating or using a gaz injection system with a micro-capillary. The sensitivity of the transducer will also be an important aspect, as the scattering cross-section will be much smaller than those of millimetric bubbles. However, this is not expected to be a critical issue; indeed, with sensitive transducers and amplifiers, it has already been demonstrated that it is possible to detect single micrometric bubbles, not only in controlled experiments [31] but also in vivo through the skull [21]. Note that a standard focused single-element MHz transducer could be used to both excite and detect sound from the bubble probe, which would result in a more compact setup as compared to our proof-of-concept setup with a hydrophone and a speaker.

The method inherently offers various contrast mechanisms, as the different resonance parameters of the bubble are influenced by the surrounding environment in a specific way. In our work, the contrast of reconstructed images is mostly driven by the frequency shift experienced by the bubble. This differs from analogue optical experiments implemented with fluorescent emitters [10–12], which are essentially sensitive to fluorescence lifetime variations and for which the frequency shift is too small to be detected. In analogy with these experi-

ments, we could also in theory measure variations of the radiative linewidth [36], which is directly related to the local density of acoustic states [48, 49]. However, the predominance of non-radiative damping in our experiments currently prevents us to measure radiative linewidth variations that are induced by the acoustic environment. Indeed, while a quality factor of around 74 is expected from the theoretical expression of the radiative linewidth $\Gamma_0 = 2\pi^2 f_0^2 d_0 / c_l$ [19], we actually typically measure a quality factor of around 10 in our experiments. This difference clearly indicates the predominance of non-radiative damping, and further investigations will be necessary to identify the underlying sources of losses. Indeed, in addition to the contribution of the thermal boundary layer, we suspect that the presence of the cage also contributes to the non-radiative damping of the bubble, an effect that could potentially be mitigated with a different cage design.

To summarize, we introduced an approach to measure acoustic interactions in the near field of complex materials with a single resonating bubble, and we experimentally demonstrated super-resolution acoustic imaging of structured samples with a resolution two orders of magnitude smaller than the wavelength of the acoustic field. This approach can be used to probe acoustic properties of structured materials as well as soft tissues without mechanical contact, therefore providing interesting perspectives for acoustic microrheology [50–52]. Moreover, we highlight that the approach can be extended to the manipulation of several bubbles, opening up interesting perspectives for the study of multiple scattering and cooperative emission phenomena in complex acoustic environments and metamaterials [53–56].

METHODS

Fabrication of the cages

Cubic cages are fabricated using a 3D printing technique based on digital light processing. A commercial resin (Monocure 3D, Grey Resin) is polymerized using a Photon Mono X (4K) Anycubic printer. Cubic cages with supports (see Fig. 1a) are designed using a computer-aided design (CAD) software (FreeCad) and saved as STereoLithography (STL) files. These files are sliced in the vertical (z) direction, with a layer thickness of 0.05 mm. The printer is operated with a normal exposure time of 2 s, a bottom exposure time of 40 s, a z -lift distance of 6 mm, a z -lift speed of 3 mm/s, a z -retract speed of 3 mm/s, and a number of bottom layers (hooking at the printing platform) of 6. Objects are fabricated layer by layer, with an upside-down orientation, resulting in a manufacturing time of around 40 minutes. After printing, the objects are rinsed in 2-propanol for 30 minutes. With a platform area of 20 cm \times 13 cm, twenty cages can be fabricated in one run. To ensure an efficient hydrophobicity of the structure, an additional

water-repellent treatment (Glaco) is applied on the dried structures. The cages that we built have an external size of 3 mm, with a pillar thickness of 0.5 mm. As the water-air interfaces are typically located on the external faces of the cages [32], the volume of air trapped inside the cages is $V \simeq 20 \text{ mm}^3$, which yields an effective bubble size of $a_0 = V^{1/3} \simeq 2.7 \text{ mm}$ and an effective spherical bubble diameter of $d_{\text{eq}} = (6V/\pi)^{1/3} \simeq 3.4 \text{ mm}$.

Experimental setup

Immersing a hydrophobic 3D-printed cage inside a tank filled with demineralized water (internal dimensions of the tank: 190 mm \times 190 mm \times 190 mm) directly leads to the formation of a bubble within the cage. The position of this caged bubble is then controlled using a 3D motorized stage (Newport ILS200PP). An arbitrary wavefront generator (Tiepie Handyscope HS5) is used to generate input electrical signals sampled at 500 kHz, at a repetition rate of 35 Hz, with a 14 bits resolution and with a maximum amplitude of $\pm 1.8 \text{ V}$. Each input signal is a Gaussian pulse, centered at 2 kHz and with a -3 dB bandwidth of 0.7 kHz. An underwater loudspeaker (Visaton FR 8 WP) fixed on the side of the tank converts this signal into an acoustic signal, which excites the bubble inside the tank. A transducer (Brüel & Kjær Miniature Hydrophone Type 8103) is used to convert the acoustic signal into an electrical signal, and also serves to hold the 3D-printed cage structure (see Fig. 1a). This signal is amplified by an amplifier (Brüel & Kjær Conditioning Amplifier Type 2692, bandpass filter 10 Hz/10 kHz, sensitivity 10 mV/Pa) before being transmitted to a USB oscilloscope (Tiepie Handyscope HS5), recording the measured signal during 25 ms at a sampling rate of 200 kHz with a 16 bits resolution.

Description of the samples

To measure variations of the bubble dynamics close to a water-steel interface, we place a stainless-steel block (block dimensions: 100 mm \times 100 mm \times 30 mm) at the bottom of the tank. In the case of the water-air interface, we simply revert the orientation of the probe (see Fig. 2e), in order to be able to place it in the vicinity of the water-air interface (interface area: 190 mm \times 190 mm).

The sample with the representation of the Eiffel tower (see Fig. 4c) is engraved in a stainless-steel plate of dimensions 153 mm \times 98 mm \times 8 mm. The fabrication process is based on water jet cutting with computer numerical control (CNC), with engraved patterns going through the whole plate thickness for this sample.

The sample with the acronym SNAM (see Fig. 4f) is engraved in a stainless-steel plate of dimensions 159 mm \times 73 mm \times 8 mm. By CNC drilling, we engrave patterns over a thickness of 7 mm, leaving a thin continuous layer of steel at the bottom of the plate (this ensures that the

central part of the letter “A” remains linked to the other part of the structure). We then cover this letter with adhesive tape (approximate thickness of 30 μm), preventing water to infiltrate in the engraved area.

The sample with three lines (see Fig. 5a) is engraved in a stainless-steel plate of dimensions 70 mm \times 65 mm \times 8 mm. By CNC drilling, we engrave three lines of equal height (42 mm) and of width equal to 3 mm, 5 mm, and 7 mm, respectively. Engraved patterns go through the whole plate thickness for this sample.

Acquisition procedure

The 1D line scans shown in Fig. 2d,h are composed of 61 equally-spaced measurements points. For these measurements, the step size is 0.5 mm, and each data point is obtained by averaging over 200 measurements to reduce the influence of noise fluctuations. The cage is first placed in contact with the interface, and the first data point is taken after moving the bubble 1 mm away from the interface. Considering that the length of the cage side is 3 mm, the first data point is thus taken at a distance $z = 2.5$ mm to the interface (the distance is defined from the interface to the estimated position of the center of the bubble). Note that, due to the low signal-to-noise ratio of the first data point in the case of the water-air interface, we removed this point and show data only starting from $z = 3$ mm.

The images of the Eiffel tower (Fig. 4d,e) are composed of 33 \times 61 measurements points, and the images of the SNAM acronym (Fig. 4g,h) are composed of 69 \times 27 measurements points. In both cases, the step size is 2 mm, and each data point is obtained by averaging over 20 measurements. The cage is first placed in contact with the sample, and then retracted by 1 mm before scanning the probe in the transverse plane; the center of the bubble is thus at a distance $z = 2.5$ mm from the interface. Raster-scans are then performed with the fast scanning direction along the longest dimension of the sample under study (the vertical dimension for the Eiffel tower, and the horizontal dimension for the SNAM acronym).

The 1D line scans shown in Fig. 5a are composed of 49 equally-spaced measurements points. For these measurements, the step size is 1 mm, and at each position we perform 200 measurements of the same field, in order to obtain different noise realizations as needed for the FRC-inspired analysis. The cage is first placed in contact with the interface, and the first line scan is performed after retracting the cage by 1 mm, which corresponds to a distance $z = 2.5$ mm. We then repeat this procedure for different values of z , ranging from $z = 2.5$ mm to $z = 8.5$ mm.

In all experiments, we first measure the field at each position in the presence of the bubble $\phi_w(\mathbf{r}, t)$. This is simply achieved by immersing a dry cage into the water tank; this cage then naturally confines and stabilizes an air bubble. Once the scan with the caged air bubble is

finished, we remove the air from the cage by injecting water inside the cage using a pipette. This allows us to measure the field at each position in the absence of the bubble $\phi_{w/o}(\mathbf{r}, t)$.

Data processing

From measurements of the scattered field in the time domain with the bubble $\phi_w(\mathbf{r}, t)$ and without the bubble $\phi_{w/o}(\mathbf{r}, t)$, we calculate the normalized scattering amplitude

$$A_s(\mathbf{r}, \omega) = \frac{\hat{\phi}_w(\mathbf{r}, \omega) - \hat{\phi}_{w/o}(\mathbf{r}, \omega)}{\hat{\phi}_{w/o}(\mathbf{r}, \omega)}, \quad (4)$$

where $\hat{\phi}_w(\mathbf{r}, \omega)$ and $\hat{\phi}_{w/o}(\mathbf{r}, \omega)$ denote the Fourier transforms of $\phi_w(\mathbf{r}, t)$ and $\phi_{w/o}(\mathbf{r}, t)$, respectively. In order to extract the central frequency of the resonance from the normalized power spectral density $|A_s(\mathbf{r}, \omega)|^2$, we use a Lorentzian function

$$f(\omega) = \frac{K}{2\pi} \frac{\gamma}{(\omega - \omega_0)^2 + (\gamma/2)^2}, \quad (5)$$

where K is a scaling factor, $\omega_0 = 2\pi f_0$ is the angular resonance frequency, and γ is the linewidth. These three parameters are the free parameters of the fitting procedure. We first identify the frequency associated with the maximum value of $|A_s(\mathbf{r}, \omega)|^2$, and we then fit a Lorentzian function to the data on a restricted frequency window around this maximum (we set the width of this window to 0.6 kHz). The influence of the number of measurements per data point on the measured resonance frequency is discussed in Supplementary Materials, Section 5.

FDTD simulations

Numerical simulations were implemented with a finite-difference time-domain (FDTD) resolution of the elastodynamic equations, with a freely available software developed in our group [39]. We followed an approach similar to the one implemented in our earlier works [32, 34]. In particular, we used a Cartesian mesh with a spatial step around 150 μm (see details in Supplementary Materials, Section S2), within a total simulation volume 20 \times 20 \times 20 mm^3 . Water and air were modeled as non-dissipative fluids, and the cage itself was neglected. The simulation volume was either surrounded by perfectly matched layers (PML) to mimic an unbounded medium, or by free boundary conditions to mimic the tank boundaries. Wideband pressure pulses in the kHz range (2 kHz center frequency, 100% -6 dB relative bandwidth) were propagated with and without the presence of the bubbles, analogous to the experimental situation, to derive the resonant frequency of the bubble from the pressure signals. To assess the sensitivity of the predicted resonant frequency to the various simulation parameters (including

the spatial grid step, the total simulation volume as compared to the volume of the bubble, thickness of the PML, etc...), several simulations were run with varying these parameters. The accuracy on the resonant frequency was estimated to be smaller than 1% error relative error.

DATA AVAILABILITY

The data generated in this study and Python scripts for data processing have been deposited in the Data

Repository Grenoble Alpes database with the following DOI: [10.57745/XNJB5K](https://doi.org/10.57745/XNJB5K).

ACKNOWLEDGMENTS

The authors thank Irène Wang for insightful discussions, Philippe Moreau for technical support, and Bruno Peccoud for the design of Fig. 1a. This project has received funding from the French Agence Nationale de la Recherche (ANR-23-CE42-0016).

-
- [1] L. Novotny and B. Hecht, *Principles of Nano-Optics* (Cambridge University Press, Cambridge, 2012).
- [2] E. H. Synge, A suggested method for extending microscopic resolution into the ultra-microscopic region, *The London, Edinburgh, and Dublin Philosophical Magazine and Journal of Science* **6**, 356 (1928).
- [3] D. W. Pohl, W. Denk, and M. Lanz, Optical stethoscopy: Image recording with resolution $\lambda/20$, *Applied Physics Letters* **44**, 651 (1984).
- [4] E. J. Sánchez, L. Novotny, and X. S. Xie, Near-Field Fluorescence Microscopy Based on Two-Photon Excitation with Metal Tips, *Physical Review Letters* **82**, 4014 (1999).
- [5] T. Kalkbrenner, M. Ramstein, J. Mlynek, and V. Sandoghdar, A single gold particle as a probe for apertureless scanning near-field optical microscopy, *Journal of Microscopy* **202**, 72 (2001).
- [6] J. Michaelis, C. Hettich, J. Mlynek, and V. Sandoghdar, Optical microscopy using a single-molecule light source, *Nature* **405**, 325 (2000).
- [7] R. J. Hermann and M. J. Gordon, Nanoscale Optical Microscopy and Spectroscopy Using Near-Field Probes, *Annual Review of Chemical and Biomolecular Engineering* **9**, 365 (2018).
- [8] P. Anger, P. Bharadwaj, and L. Novotny, Enhancement and Quenching of Single-Molecule Fluorescence, *Physical Review Letters* **96**, 113002 (2006).
- [9] S. Kühn, U. Håkanson, L. Rogobete, and V. Sandoghdar, Enhancement of Single-Molecule Fluorescence Using a Gold Nanoparticle as an Optical Nanoantenna, *Physical Review Letters* **97**, 017402 (2006).
- [10] M. Frimmer, Y. Chen, and A. Koenderink, Scanning Emitter Lifetime Imaging Microscopy for Spontaneous Emission Control, *Physical Review Letters* **107**, 123602 (2011).
- [11] L. Aigouy, A. Cazé, P. Gredin, M. Mortier, and R. Carninatti, Mapping and Quantifying Electric and Magnetic Dipole Luminescence at the Nanoscale, *Physical Review Letters* **113**, 076101 (2014).
- [12] D. Bouchet, M. Mivelle, J. Proust, B. Gallas, I. Ozerov, M. F. Garcia-Parajo, A. Gulinatti, I. Rech, Y. De Wilde, N. Bonod, V. Krachmalnicoff, and S. Bidault, Enhancement and Inhibition of Spontaneous Photon Emission by Resonant Silicon Nanoantennas, *Physical Review Applied* **6**, 064016 (2016).
- [13] P. N. T. Wells, Ultrasound imaging, *Physics in Medicine & Biology* **51**, R83 (2006).
- [14] D. Ensminger and L. J. J. Bond, *Ultrasonics: Fundamentals, Technologies, and Applications* (CRC Press, 2024).
- [15] P. Günther, U. C. Fischer, and K. Dransfeld, Scanning near-field acoustic microscopy, *Applied Physics B* **48**, 89 (1989).
- [16] U. Rabe and W. Arnold, Acoustic microscopy by atomic force microscopy, *Applied Physics Letters* **64**, 1493 (1994).
- [17] L. Langguth, R. Fleury, A. Alù, and A. F. Koenderink, Drexhage's Experiment for Sound, *Physical Review Letters* **116**, 224301 (2016).
- [18] M. K. Schmidt, L. Helt, C. G. Poulton, and M. Steel, Elastic Purcell Effect, *Physical Review Letters* **121**, 064301 (2018).
- [19] T. G. Leighton, *The Acoustic Bubble* (Academic Press, San Diego, 1997).
- [20] B. Dollet, P. Marmottant, and V. Garbin, Bubble Dynamics in Soft and Biological Matter, *Annual Review of Fluid Mechanics* **51**, 331 (2019).
- [21] C. Errico, J. Pierre, S. Pezet, Y. Desailly, Z. Lenkei, O. Couture, and M. Tanter, Ultrafast ultrasound localization microscopy for deep super-resolution vascular imaging, *Nature* **527**, 499 (2015).
- [22] E. Betzig, G. H. Patterson, R. Sougrat, O. W. Lindwasser, S. Olenych, J. S. Bonifacino, M. W. Davidson, J. Lippincott-Schwartz, and H. F. Hess, Imaging Intracellular Fluorescent Proteins at Nanometer Resolution, *Science* **313**, 1642 (2006).
- [23] G. Zhang, S. Harput, S. Lin, K. Christensen-Jeffries, C. H. Leow, J. Brown, C. Dunsby, R. J. Eckersley, and M.-X. Tang, Acoustic wave sparsely activated localization microscopy (awsalm): Super-resolution ultrasound imaging using acoustic activation and deactivation of nanodroplets, *Applied Physics Letters* **113** (2018).
- [24] R. R. Dagastine, G. W. Stevens, D. Y. C. Chan, and F. Grieser, Forces between two oil drops in aqueous solution measured by AFM, *Journal of Colloid and Interface Science* **273**, 339 (2004).
- [25] R. R. Dagastine, R. Manica, S. L. Carnie, D. Y. C. Chan, G. W. Stevens, and F. Grieser, Dynamic Forces Between Two Deformable Oil Droplets in Water, *Science* **313**, 210 (2006).
- [26] I. U. Vakarelski, J. Lee, R. R. Dagastine, D. Y. C. Chan, G. W. Stevens, and F. Grieser, Bubble Colloidal AFM Probes Formed from Ultrasonically Generated Bubbles, *Langmuir* **24**, 603 (2008).
- [27] I. U. Vakarelski, R. Manica, X. Tang, S. J. O'Shea, G. W. Stevens, F. Grieser, R. R. Dagastine, and D. Y. C. Chan,

- Dynamic interactions between microbubbles in water, *Proceedings of the National Academy of Sciences* **107**, 11177 (2010).
- [28] C. Shi, X. Cui, L. Xie, Q. Liu, D. Y. C. Chan, J. N. Israelachvili, and H. Zeng, Measuring Forces and Spatiotemporal Evolution of Thin Water Films between an Air Bubble and Solid Surfaces of Different Hydrophobicity, *ACS Nano* **9**, 95 (2015).
- [29] C. Qiao, D. Yang, X. Mao, L. Xie, L. Gong, X. Peng, Q. Peng, T. Wang, H. Zhang, and H. Zeng, Recent advances in bubble-based technologies: Underlying interaction mechanisms and applications, *Applied Physics Reviews* **8**, 011315 (2021).
- [30] V. Garbin, D. Cojoc, E. Ferrari, E. Di Fabrizio, M. L. J. Overvelde, S. M. van der Meer, N. de Jong, D. Lohse, and M. Versluis, Changes in microbubble dynamics near a boundary revealed by combined optical micromanipulation and high-speed imaging, *Applied Physics Letters* **90**, 114103 (2007).
- [31] B. L. Helfield, B. Y. C. Leung, and D. E. Goertz, The effect of boundary proximity on the response of individual ultrasound contrast agent microbubbles, *Physics in Medicine & Biology* **59**, 1721 (2014).
- [32] M. Harazi, M. Rupin, O. Stephan, E. Bossy, and P. Marmottant, Acoustics of Cubic Bubbles: Six Coupled Oscillators, *Physical Review Letters* **123**, 254501 (2019).
- [33] T. Combriat, P. Rouby-Poizat, A. A. Doinikov, O. Stephan, and P. Marmottant, Acoustic interaction between 3D-fabricated cubic bubbles, *Soft Matter* **16**, 2829 (2020).
- [34] M. Boughzala, O. Stephan, E. Bossy, B. Dollet, and P. Marmottant, Polyhedral Bubble Vibrations, *Physical Review Letters* **126**, 054502 (2021).
- [35] M. Alloul, B. Dollet, O. Stephan, E. Bossy, C. Quiliet, and P. Marmottant, Acoustic Resonance Frequencies of Underwater Toroidal Bubbles, *Physical Review Letters* **129**, 134501 (2022).
- [36] A. A. Doinikov, L. Aired, and A. Bouakaz, Acoustic scattering from a contrast agent microbubble near an elastic wall of finite thickness, *Physics in Medicine & Biology* **56**, 6951 (2011).
- [37] M. Morioka, Theory of Natural Frequencies of Two Pulsating Bubbles in Infinite Liquid, *Journal of Nuclear Science and Technology* **11**, 554 (1974).
- [38] M. Strasberg, The Pulsation Frequency of Nonspherical Gas Bubbles in Liquids, *The Journal of the Acoustical Society of America* **25**, 536 (1953).
- [39] E. Bossy, M. Talmant, and P. Laugier, Three-dimensional simulations of ultrasonic axial transmission velocity measurement on cortical bone models, *The Journal of the Acoustical Society of America* **115**, 2314 (2004).
- [40] H. H. Barrett and K. J. Myers, *Foundations of Image Science* (John Wiley & Sons, 2003).
- [41] W. O. Saxton and W. Baumeister, The correlation averaging of a regularly arranged bacterial cell envelope protein, *Journal of Microscopy* **127**, 127 (1982).
- [42] M. Van Heel, Similarity measures between images, *Ultra-microscopy* **21**, 95 (1987).
- [43] R. P. J. Nieuwenhuizen, K. A. Lidke, M. Bates, D. L. Puig, D. Grünwald, S. Stallinga, and B. Rieger, Measuring image resolution in optical nanoscopy, *Nature Methods* **10**, 557 (2013).
- [44] N. Banterle, K. H. Bui, E. A. Lemke, and M. Beck, Fourier ring correlation as a resolution criterion for super-resolution microscopy, *Journal of Structural Biology* **183**, 363 (2013).
- [45] E. G. Williams, *Fourier Acoustics: Sound Radiation and Nearfield Acoustical Holography* (Academic Press, San Diego, 1999).
- [46] M. Carloti and V. Mattoli, Functional Materials for Two-Photon Polymerization in Microfabrication, *Small* **15**, 1902687 (2019).
- [47] P. Anastasiadis and P. V. Zinin, High-Frequency Time-Resolved Scanning Acoustic Microscopy for Biomedical Applications, *The Open Neuroimaging Journal* **12**, 69 (2018).
- [48] R. Carminati, A. Cazé, D. Cao, F. Peragut, V. Krachmalnicoff, R. Pierrat, and Y. De Wilde, Electromagnetic density of states in complex plasmonic systems, *Surface Science Reports* **70**, 1 (2015).
- [49] M. Landi, J. Zhao, W. E. Prather, Y. Wu, and L. Zhang, Acoustic Purcell Effect for Enhanced Emission, *Physical Review Letters* **120**, 114301 (2018).
- [50] A. Strybulevych, V. Leroy, M. G. Scanlon, and J. H. Page, Acoustic Microrheology : Shear Moduli of Soft Materials Determined from Single Bubble Oscillations, *Proceedings of Symposium on Ultrasonic Electronics* **30**, 395 (2009).
- [51] F. Hamaguchi and K. Ando, Linear oscillation of gas bubbles in a viscoelastic material under ultrasound irradiation, *Physics of Fluids* **27**, 113103 (2015).
- [52] A. Jamburidze, M. D. Corato, A. Huerre, A. Pommella, and V. Garbin, High-frequency linear rheology of hydrogels probed by ultrasound-driven microbubble dynamics, *Soft Matter* **13**, 3946 (2017).
- [53] A. Tourin, M. Fink, and A. Derode, Multiple scattering of sound, *Waves in Random Media* **10**, R31 (2000).
- [54] V. Leroy, A. Strybulevych, M. Lanoy, F. Lemoult, A. Tourin, and J. H. Page, Superabsorption of acoustic waves with bubble metascreens, *Physical Review B* **91**, 020301 (2015).
- [55] S. A. Cummer, J. Christensen, and A. Alù, Controlling sound with acoustic metamaterials, *Nature Reviews Materials* **1**, 1 (2016).
- [56] G. Ma and P. Sheng, Acoustic metamaterials: From local resonances to broad horizons, *Science Advances* **2**, e1501595 (2016).

Near-field acoustic imaging with a caged bubble

Supplementary information

Dorian Bouchet,¹ Olivier Stephan,¹ Benjamin Dollet,¹ Philippe Marmottant,¹ and Emmanuel Bossy¹

¹ *Université Grenoble Alpes, CNRS, LIPhy, 38000 Grenoble, France*

S1. TEMPORAL DRIFT OF THE RESONANCE FREQUENCY

During an acquisition, the volume of air in a bubble tends to slightly decrease over time, leading to a slight increase of the resonance frequency of the bubble over time. To characterize this effect, we present in Fig. S1 the resonance frequency of different bubbles in the absence of sample, as a function of time. All measurements were performed with the same 3D-printed cage, but due to a variability in the process of bubble formation by immersion of the cage, each bubble is characterized by a slightly different volume, resulting in different resonance frequencies. Moreover, air is progressively lost by the bubbles over time, resulting in a slow increase in the observed resonance frequencies. Note that the rate at which air escapes the cage can also vary, which may arise due to variations in the wettability of the cage, that is not precisely controlled during the immersion of the cage.

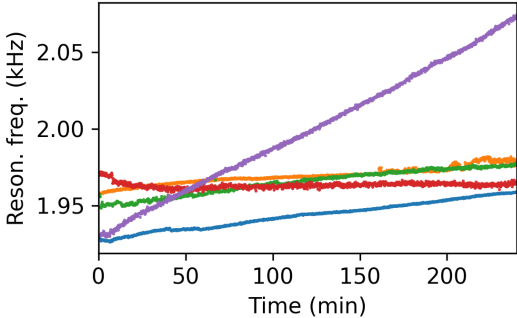


FIG. S1. Temporal drift of the resonance frequency. Resonance frequency of different bubbles in the absence of sample, as a function of time. The different colors represent different measurements. Before each measurement, the 3D-printed cage is dried before being immersed into water. A new bubble is thus formed inside the cage prior to each measurement. For each measurement, there are small variations in the amount of air trapped into the cage, resulting in slightly different resonance frequencies.

This effect can be significant on long acquisitions, such as those presented in Fig. 4 of the manuscript. For the image of the Eiffel tower (acquisition time of 1 hour and 58 min), the resonance frequency of the bubble in the vicinity of steel increased from 1.78 kHz to 1.79 kHz over the whole acquisition. For the image of the SNAM acronym (acquisition time of 1 hour and 49 min), the resonance frequency of the bubble in the vicinity of steel increased from 1.69 kHz to 1.79 kHz over the whole acquisition. To correct for this effect, we simply assume that the resonance frequency varies linearly in time, and we apply a correction to all measured resonance frequencies, taking as a reference the central frequency extracted from the power spectral density measured at the beginning of the experiment (i.e., the first point of the scan). The uncorrected images are presented in Fig. S2. While this correction does not significantly affect the reconstructed image of the Eiffel tower, we can see that it does affect the image of the SNAM acronym. On the uncorrected image of the SNAM acronym sample (Fig. S2c), the resonance frequency is indeed higher for the data points that have been measured at the end of the acquisition (lower right corner) as compared to those that have been measured at the beginning of the acquisition (upper left corner). Overall, this strategy allows performing long acquisitions with the same bubble (up to dozens of hours).

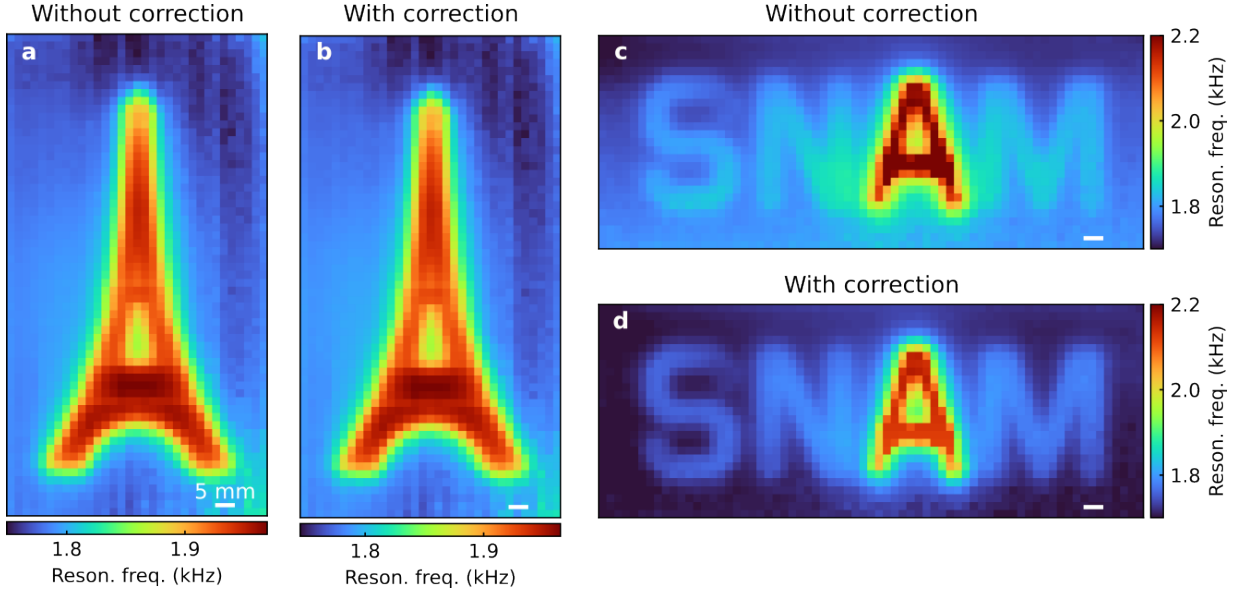


FIG. S2. Correction applied on the frequency images. Images of the measured central frequencies, before (a,c) and after (b,d) correcting for the slow decrease in the gas volume inside the bubble. The correction simply consists in measuring the frequency shift during the acquisition from measurements of the same data point before and after the acquisition, and performing a linear interpolation to estimate the frequency shift during the acquisition. Scale bar: 5 mm.

S2. FINITE-DIFFERENCE TIME-DOMAIN SIMULATIONS

S2.1. Bubble dynamics close to interfaces for spherical and cubic bubbles

FDTD results that we presented in the manuscript were normalized: the resonance frequency was normalized by the homogeneous-space resonance frequency, and the bubble-to-interface distance was normalized by the effective bubble diameter. In this section, we present non-normalized results, in order to compare the resonance frequency of spherical and cubic bubbles of identical volume. Simulations with cubic bubbles were performed with a length size $a_0 = 2.5$ mm

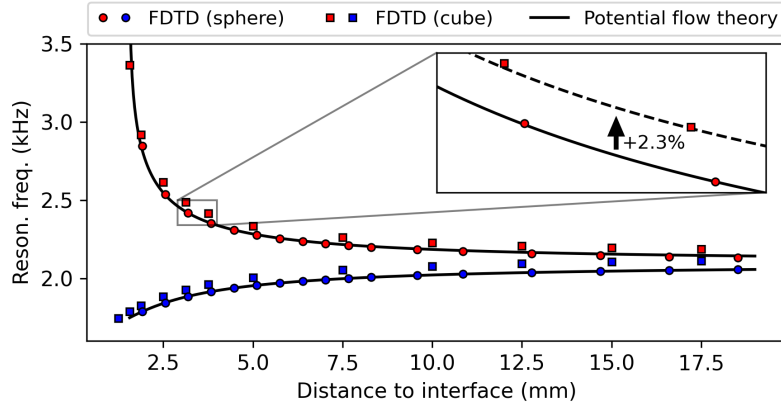


FIG. S3. Resonance frequency for spherical and cubic bubbles. Relation between the resonance frequency and the bubble-interface distance for rigid (in blue) and free (in red) interfaces. Theoretical predictions obtained using Eq. (2) of the manuscript are represented by black lines. Results of FDTD simulations performed with a spherical bubble in water surrounding by perfectly-matched layers are represented by blue and red circles. Results of FDTD simulations performed with a cubic bubble in water enclosed in a finite tank are represented by blue and red squares. These simulations have been performed so that the volume of the spherical bubble matches the volume of the cubic one.

($16 \times 16 \times 16 = 4096$ pixels, mesh size = 0.15625 mm, volume of 15.625 mm^3). Simulations with spherical bubbles were performed with a the same exact volume. Note that because of the discretization over a Cartesian mesh, matching the volume of an approximate discretized sphere to an exact value required us to slightly tune the mesh size: our discretized sphere had 4032 pixels, imposing a mesh size of 0.15707 mm in order to reach a volume of 15.625 mm^3 .

Results are presented in Fig. S3, for both a spherical bubble surrounded by perfectly matched layers and a cubic bubbles inside a finite tank. The resonance frequency observed for the spherical bubble surrounded by perfectly matched layers almost exactly matches the one obtained using the expression derived by Morioka based on the potential flow of an incompressible liquid [1], which describes the case of a spherical bubble close to an interface separating two semi-infinite media. This evidences that neglecting the compressibility of the flow is an excellent approximation in the near-field of the bubble, as our FDTD simulations do take into account the finite compressibility in the fluid. In comparison, the resonance frequency observed for the cubic bubble in the finite tank is slightly larger (approximately 2.3%). A similar effect has been observed in a previous work [2], in which a 2.6% increase of the homogeneous-space resonance frequency was reported for a cubic bubble as compared to a spherical one. This indicates that the different bubble geometry is the dominant effect to explain the small increase in the resonance frequency observed for cubic bubbles. The influence of the finite tank is smaller in comparison, as we further verified by conducting additional numerical simulations with cubic bubbles surrounded by perfectly-matched layers (no significant differences were observed as compared to the case of the cubic bubble in the finite tank).

S2.2. Instantaneous pressure fields around spherical and cubic bubbles

At any given time in the FDTD simulations, we can record a snapshot of the pressure field around the bubble. In Fig. S4, we show the normalized pressure field around cubic and spherical bubbles, in the vicinity of rigid and free interfaces. These snapshots were recorded at the first maximum of the oscillating field after the exciting field has vanished. Note that other times could have been chosen, as the normalized pressure field is essentially the same at any given time after the exciting field has vanished.

On these snapshots, it clearly appears that the field is affected by the detailed geometry of the bubble only in its very close vicinity, and that the fields generated by cubic and spherical bubbles are very similar as soon as they are evaluated at distances larger than the bubble size. In this regime, we can conclude that the fields are essentially those that would be generated by two in-phase monopoles (rigid interface) or two out-of-phase monopoles (free interface).

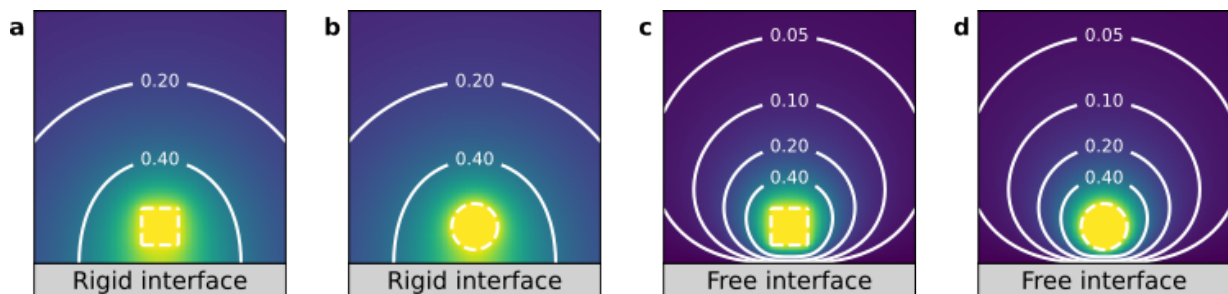


FIG. S4. Pressure fields around spherical and cubic bubbles. **a,b**, Normalized instantaneous pressure fields calculated by FDTD around a cubic bubble **a**, and a spherical bubble **b**, close to a rigid interface. **c,d**, Analogous to **a,b** for bubbles close to a free interface. On these figures, the edges of the bubble are represented by dotted white lines, and the edge size of the whole field of view is 17.2 mm.

S3. MULTISPECTRAL IMAGES

In the manuscript, we described two imaging modes that provide different image contrasts, namely, intensity imaging (see Fig. 4a of the manuscript) and central frequency imaging (see Fig. 4b of the manuscript). However, in the intensity imaging mode, the choice of the frequency at which the image is formed is arbitrary. In the manuscript, we chose to present images measured at a frequency close to the natural resonance frequency of the bubble in water ($f = 1.96 \text{ kHz}$), but other choices are possible. Thus, for the sake of completeness, we present here the intensity images obtained at various frequencies ranging from 1.48 kHz to 2.40 kHz.

S3.1. The Eiffel tower sample

In Fig. S5, we show multispectral images measured for the Eiffel tower sample. For frequencies smaller than 1.88 kHz, we observe that the intensity scattered by the bubble is stronger when the bubble is above stainless steel, which is due to the large negative frequency shift experienced by the bubble in these areas. In contrast, for frequencies larger than 1.88 kHz, we observe that the intensity scattered by the bubble is stronger when the bubble is above areas filled with water, for which the resonance frequency is less shifted.

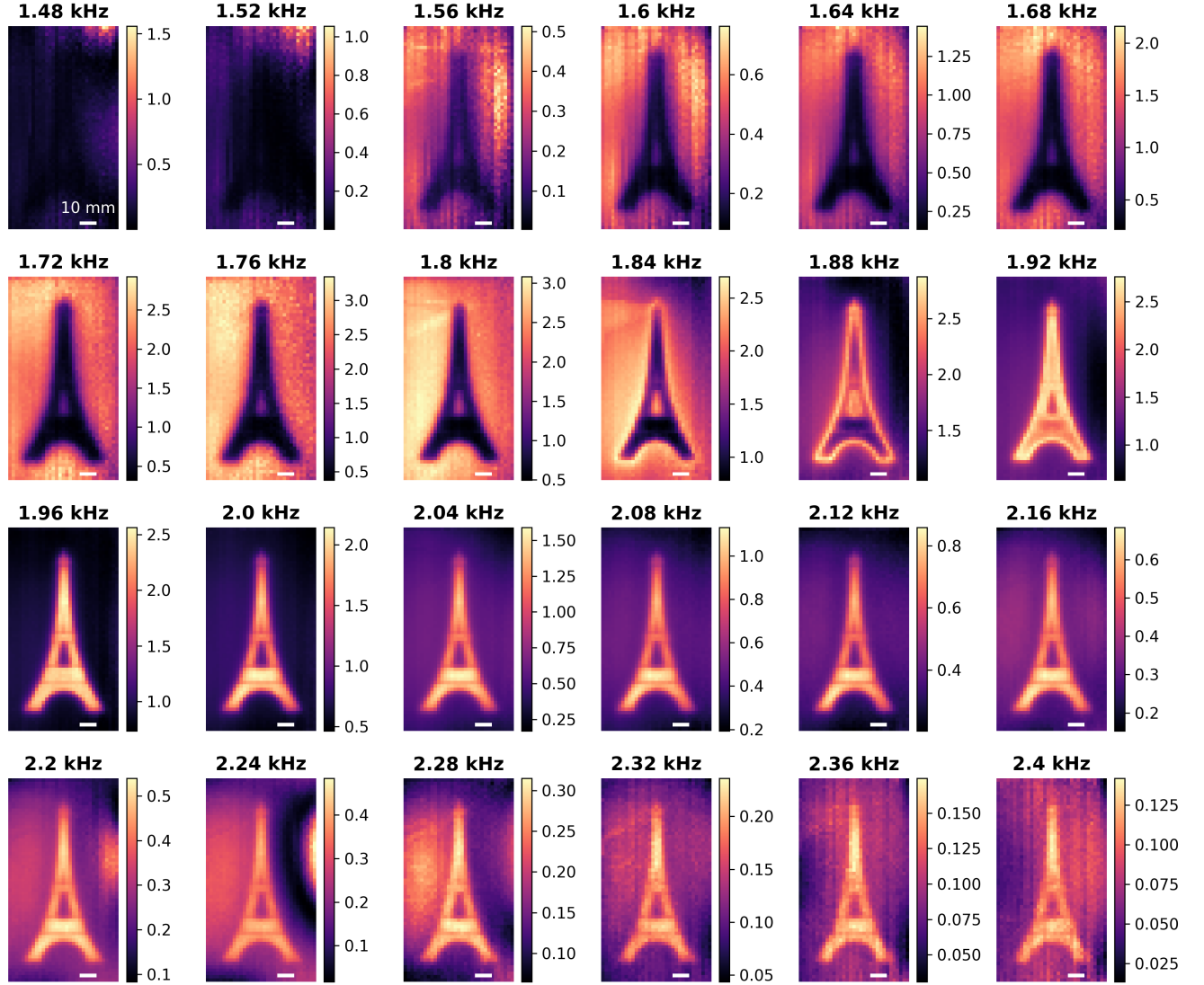


FIG. S5. Multispectral intensity images of the Eiffel tower sample. Power spectral density of the scattered field for different frequencies ranging from 1.48 kHz to 2.4 kHz. The contrast of the images is inverted as the imaging frequency is increased: low frequency images highlight the areas above which the resonance frequency of the bubble is lower (i.e., when the bubble is above stainless steel), while high frequency images highlight the areas above which the resonance frequency is higher (i.e., when the bubble is above areas filled with water). Scale bar: 10 mm.

S3.2. The SNAM acronym sample

In Fig. S6, we show multispectral images measured for the SNAM acronym sample. For frequencies larger than 2.12 kHz, we observe that the intensity scattered by the bubble is stronger when the bubble is above areas filled with air (i.e. the letter “A”), which is due to the large positive frequency shift experienced by the bubble in these areas. For frequencies in-between 1.76 kHz and 2.12 kHz, the intensity scattered by the bubble is stronger when the bubble is above areas filled with water (i.e. the letters “S”, “N” and “M”); in this range, the resonance frequency of the bubble is weakly influenced by its environment. Finally, for frequencies below 1.76 kHz, we observe that the intensity scattered by the bubble is stronger when the bubble is above stainless steel, which is due to the large negative frequency shift experienced by the bubble in these areas.

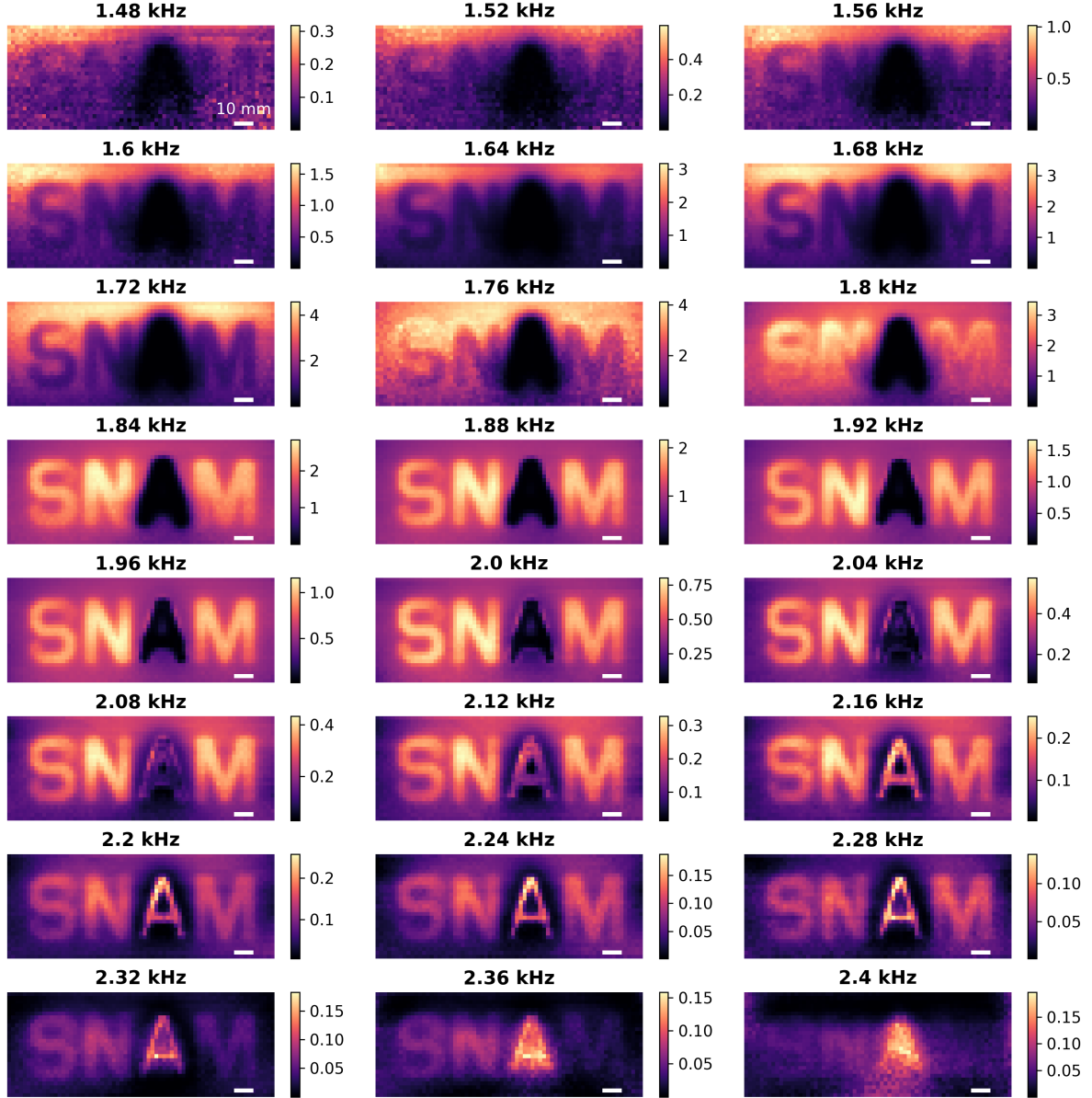


FIG. S6. Multispectral images of the SNAM acronym sample. Power spectral density of the scattered field for different frequencies ranging from 1.48 kHz to 2.4 kHz. The letter “A”, which is filled with air, is especially visible at high frequencies, as expected for a bubble resonating above a free interface. At lower frequencies, this letter is not visible, as the measured signal scattered by the bubble is very weak above a water-air interface. Scale bar: 10 mm.

S4. TRANSVERSE RESOLUTION AS A FUNCTION OF THE BUBBLE-SAMPLE DISTANCE

In order to quantify the transverse resolution of the technique, we adopt a strategy inspired by Fourier ring correlation (FRC), which provides a resolution criterion that can be computed directly from experimental data [3–6]. The method is based on n statistically-independent measurements of some raw data taken as a function of spatial coordinates, either in 1D (a line scan) or in 2D (an image scan). Here, we consider as raw data the fields measured in the presence of the bubble during a 1D line scan performed above a resolution test sample composed of three grooves (see Figure 5a of the manuscript). We denote this data set $\phi_w^{(i)}(x, t)$, where i denotes the index of the noise realization. We then successively apply a temporal discrete Fourier transform and a spatial discrete Fourier transform to these data, which results in a data set noted $\hat{\phi}_w^{(i)}(k_x, \omega)$. As an illustration, we show in Fig. S7a two independent measurements extracted from this data set, taken for a bubble-sample distance $z = 2.5$ mm. We observe that, while noise weakly affects low spatial frequencies, it strongly corrupts high spatial frequencies.

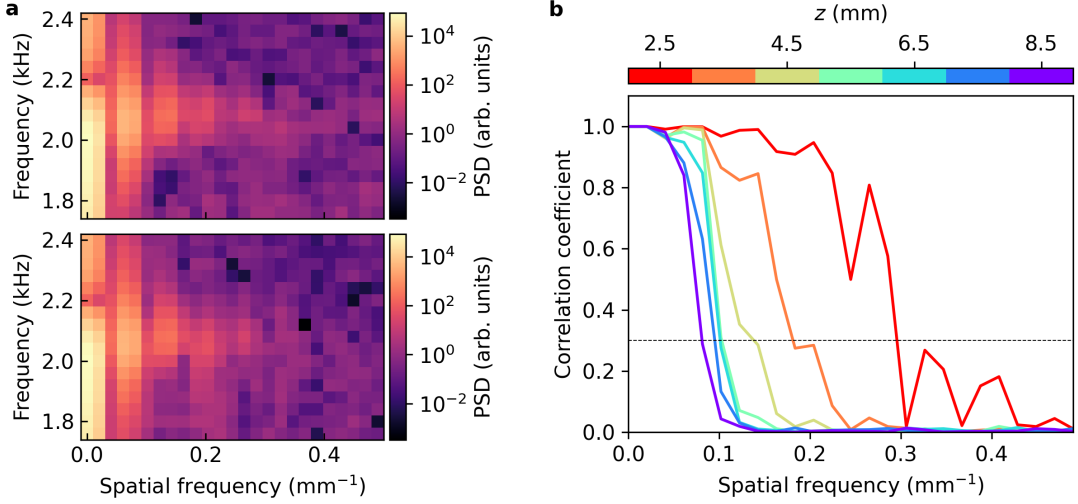


FIG. S7. Determination of the transverse resolution of the approach. **a**, Power spectral density measured in the presence of the bubble, with the temporal frequency in the vertical axis and the spatial frequency in the horizontal axis. This was obtained by Fourier transforming the field measured during a 1D line scan performed above a resolution test sample composed of three lines (see Figure 5a of the manuscript). The top and bottom sub-figures represent two identical measurements performed in the presence of noise. Noise weakly affects low spatial frequencies, but strongly corrupts high spatial frequencies. **b**, Absolute value of the mean correlation coefficient calculated by correlating the power spectral densities measured for each spatial frequency. For each distance z , the signals have been measured 200 times with different noise realizations, and the average has been calculated over 19900 different pairs. By setting an arbitrary threshold (here equal to 0.3), we can calculate the maximal spatial frequency ξ contained in these 1D line scans (see Figure 5b of the manuscript).

By calculating the correlation coefficient between such measurements as a function of k_x , we can assess which spatial frequencies are robust to noise fluctuations, and which spatial frequencies are dominated by noise. We use the following expression for the mean correlation coefficient:

$$C(k_x) = \frac{1}{n(n-1)/2} \sum_{(i,j) \in \mathcal{P}} \frac{\sum_{l \in \mathcal{Q}} \hat{\phi}_w^{(i)}(k_x, \omega_l) [\hat{\phi}_w^{(j)}(k_x, \omega_l)]^*}{\sqrt{\sum_{l \in \mathcal{Q}} |\hat{\phi}_w^{(i)}(k_x, \omega_l)|^2} \sqrt{\sum_{l \in \mathcal{Q}} |\hat{\phi}_w^{(j)}(k_x, \omega_l)|^2}}, \quad (\text{S1})$$

where \mathcal{P} denotes the ensemble of all possible pairs of noise realizations and \mathcal{Q} denotes the ensemble of all temporal frequencies for which the signal coming from the bubble is significant. In practice, the signals have been measured $n = 200$ times with different noise realizations, and thus the average over noise realization has been calculated over $n(n-1)/2 = 19900$ pairs. The sums over temporal frequencies run from 1.75 kHz to 2.45 kHz for these measurements. Finally, note that a Hann window was applied to the data along the spatial dimension before applying the spatial discrete Fourier transform in order to avoid spectral leakage.

The amplitude of the measured correlation coefficient is shown in Fig. S7b for different bubble-sample distances z . We observe that the correlation coefficient is close to unity for small spatial frequencies, and tends to zero for large spatial frequencies. Moreover, larger spatial frequencies are observed for smaller values of z , which supports

the observation that the resolution rapidly degrades with the bubble-sample distance. In order to extract a single resolution criterion from these data, we identify the cutoff frequency ξ such that $|C(\xi)| = 0.3$, where the threshold value 0.3 has been chosen arbitrarily to distinguish signal from noise. Note that results only weakly depend of this threshold value, as the correlation coefficient rapidly drops from 1 to 0 for each value of z . Finally, the resolution is simply calculated as the inverse of the observed cutoff frequency ($\mathcal{R} = 1/\xi$).

S5. NUMBER OF MEASUREMENTS PER DATA POINT

In this section, we compare the signal-to-noise ratio of the measured resonance frequency for different numbers of measurements per data point, taking as an example the 1D line scans performed above the resolution test sample (Fig. 5a of the manuscript). While averaging each data point over 200 measurements yields an excellent signal-to-noise ratio (Fig. S8c), averaging over 20 measurements already gives us a very good signal-to-noise ratio (Fig. S8b). Moreover, it is also possible to rely a single measurement per data point, at the cost of a degraded signal-to-noise ratio (Fig. S8a).

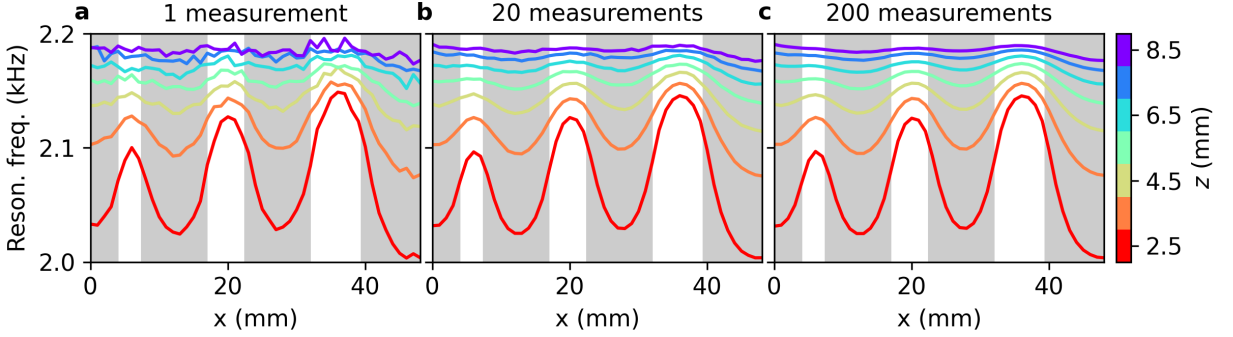


FIG. S8. Influence of the number of measurements per data point. Measurements of the resonance frequency of the bubble for the 1D line scans shown in Fig. 5a of the manuscript. The number of measurements used at each point is either 1 (a), 20 (b) or 200 (c).

In practice, in our imaging experiments, each data point was obtained by averaging over 20 measurements; even though this was not strictly necessary, it gave us a better signal-to-noise ratio without strongly affecting the total acquisition time. Indeed, taking the example of the Eiffel tower sample, the total acquisition time was 1 hour and 58 min but, during this time, only around 19 min were spent for actually measuring the data. This clearly shows that the total acquisition time is mostly due to the time spent by the motorized stage to go from position to position, and not by the measurement time.

S6. FITTING PROCEDURE

In Fig. 2d,h of the manuscript, we compare the results of the 1D line scans in the z -direction to the theoretical predictions derived by Morioka [1]. The model function is:

$$f_{\pm}(\Delta z, d_{\text{eq}}, z_0) = \left(\frac{c_g \sqrt{3\rho_g/\rho_l}}{\pi d_{\text{eq}}} \right) \times \sqrt{\sum_{n=0}^{+\infty} \frac{(\mp 1)^n \sinh(\beta)}{\sinh[(n+1)\beta]}} \quad (\text{S2})$$

where $\cosh(\beta) = 2(z_0 + \Delta z)/d_{\text{eq}}$. In Eq. (S2), the first term (inside braces) corresponds to Minnaert's formula giving the homogeneous resonance frequency, while the second term (under the square root) corresponds to Morioka's result giving the distance dependence. Note that in practice we need to truncate the series for their numerical evaluation; here we keep the first 100 terms, which is sufficient to estimate the series up to machine precision. Taking $c_g = 340 \text{ m/s}$, $\rho_g = 1.2 \text{ kg/m}^3$ and $\rho_l = 1000 \text{ kg/m}^3$, we are left with three parameters: the effective bubble diameter d_{eq} , the bubble-interface distance for the first measurement point z_0 (when the bubble is closest to the interface) and the relative displacement applied by the motorized stage for all other measurement points Δz . While Δz is precisely

controlled by the stage in the experiment, it is difficult to precisely control the value of two other parameters d_{eq} and z_0 . However, we can estimate these values directly from the data by treating them as free parameters. They are numerically determined by solving

$$d_{\text{eq}}, z_0 = \underset{d', z'}{\operatorname{argmin}} \left(\sum_i [f_{\pm}^{\text{exp}}(\Delta z_i) - f_{\pm}(\Delta z_i, d', z')]^2 \right), \quad (\text{S3})$$

where $f_{\pm}^{\text{exp}}(\Delta z_i)$ denotes the experimental results of the 1D line scans in the z -direction. In the case of the water-steel interface, we obtain an effective diameter of 3.1 mm and a bubble-interface distance z_0 of 2.3 mm. In the case of the water-air interface, we obtain an effective diameter of 3.4 mm and a bubble-interface distance z_0 of 2.6 mm. These values are consistent with what can be expected from the geometry of the cages (volume of trapped air $V \leq 20 \text{ mm}^3$, which gives $d_{\text{eq}} \leq 3.4 \text{ mm}$) and from our procedure to control the minimal bubble-interface distance ($z_0 \simeq 2.5 \text{ mm}$ by establishing the contact by eye and retracting it by 1 mm). The standard error on these values can be roughly estimated from the covariance matrices obtained using `scipy.optimize.curve_fit`; the standard errors for the estimated effective diameters are 0.001 mm (water-steel interface) and 0.0005 mm (water-air interface); the standard errors for the estimated bubble-interface distances are 0.04 mm (water-steel interface) and 0.01 mm (water-air interface).

In practice, varying z_0 amounts to horizontally translate the function f_{\pm} , and varying d_{eq} amounts to vertically translate this function (up to a very good approximation). Therefore, the precise value of these parameters have no effect on the shape of the model function. We can thus conclude that the theoretical model of Morioka, originally introduced for spherical bubbles, accurately describes the shape of the distance dependence that we experimentally observe using square bubbles.

-
- [1] M. Morioka, Theory of Natural Frequencies of Two Pulsating Bubbles in Infinite Liquid, *Journal of Nuclear Science and Technology* **11**, 554 (1974).
 - [2] M. Boughzala, O. Stephan, E. Bossy, B. Dollet, and P. Marmottant, Polyhedral Bubble Vibrations, *Physical Review Letters* **126**, 054502 (2021).
 - [3] W. O. Saxton and W. Baumeister, The correlation averaging of a regularly arranged bacterial cell envelope protein, *Journal of Microscopy* **127**, 127 (1982).
 - [4] M. Van Heel, Similarity measures between images, *Ultramicroscopy* **21**, 95 (1987).
 - [5] R. P. J. Nieuwenhuizen, K. A. Lidke, M. Bates, D. L. Puig, D. Grünwald, S. Stallinga, and B. Rieger, Measuring image resolution in optical nanoscopy, *Nature Methods* **10**, 557 (2013).
 - [6] N. Banterle, K. H. Bui, E. A. Lemke, and M. Beck, Fourier ring correlation as a resolution criterion for super-resolution microscopy, *Journal of Structural Biology* **183**, 363 (2013).